

# Lithosphere–atmosphere–ionosphere coupling during the September 2015 Coquimbo earthquake

B. Adhikari <sup>1</sup>, V. Klausner <sup>2\*</sup>, C. M. N. Cândido<sup>2</sup>, P. Poudel <sup>1</sup>, H. M. Gimenes <sup>2</sup>, A. Silwal <sup>3</sup>, S. P. Gautam <sup>4</sup>, A. Calabia<sup>5</sup>, and M. Shah

<sup>1</sup> St. Xavier's Collage, Maitighar, 44600, Kathmandu, Nepal.

<sup>2</sup> Physics and Astronomy, Vale do Paraiba University, Av. Shishima Hifumi, 2911, Brazil.

<sup>3</sup> Patan Multiple Campus, Tribhuvan University, Lalitpur, Nepal.

<sup>4</sup> Central Department of Physics, Tribhuvan University, Kirtipur, Nepal.

<sup>5</sup> School of Land Surveying, Geodesy and Mapping Engineering, Technical University of Madrid, 28031 Madrid, Spain.

<sup>6</sup> Department of Space Science, Institute of Space Technology, Islamabad, 44000, Pakistan

\*Correspondence: [virginia@univap.br](mailto:virginia@univap.br)

**Abstract:** This study explores temporal variations in seismic data, interplanetary parameters, and geomagnetic indices during the 2015 Coquimbo earthquake. We employ wavelet transform techniques to investigate potential coupling mechanisms between the lithosphere, atmosphere, and ionosphere (LAI), even during geomagnetically disturbed periods. Our analysis is strengthened by evaluating geomagnetic data and all-sky images within a 2000–3000 km radius of the epicenter. We explore the post-Chilean earthquake seismogenic perturbations in the upper atmosphere on September 16–17, 2015. Coseismic and post-seismic events emerge in the Brazilian region 1–3 hrs after the earthquake onset. The co-occurrence and subsequent response of these disturbances to seismic events suggest their seismogenic nature. Additionally, we utilize geomagnetic storm and interplanetary magnetic field (IMF) indices to differentiate magnetic fluctuations arising from solar storms during seismic events. While our study detects magnetic disturbances associated with seismic activity, distinguishing them from the effects of solar storms in the geomagnetic records or all-sky images remains challenging. These observations prompt further investigation into the intricate interplay between geomagnetic and ionospheric disturbances and their connection to seismic and geomagnetic storm activity.

**Keywords:** Lithosphere-Ionosphere Coupling; Wavelet Transform; Geomagnetic storms

## 1. Introduction

Following a decade of significant mathematical formalism, the wavelet transform (WT) is increasingly being used to investigate a large range of geophysical processes, including for example El Niño-Southern Oscillation [1], rainfall data [2,3], tropical convection [4], atmospheric turbulences [5], ocean wind waves, layered geologic structures, climate change [6,7], and the determination of earthquake parameters [8,9]. Due to its unique feature that make it well-suited to study natural processes, WT applications in geophysics are expected to evolve in the next years into a key tool for research [5,10–15].

Seismic data has a nonstationary amplitude, and the energy associated with the signal is strong at the beginning and then gradually decreases [16,17]. On the other side, the nonstationary frequency of a seismic wave is related to distinct types of seismic waves, composition of different frequencies, and spatial distribution features [17]. This non-stationarity character in physical responses has grabbed the attention of many researchers motivated by evolutionary power spectrums for slowly evolving nonstationary phenomena, where the spectral analysis is a fundamental step in the analysis. Numerous aspects inherent in the signal that are not represented by time can be detected and, to date, wavelet transform is the most appropriate tool for examining these signals at various frequencies, since it is a localized technique in both space and time. This feature is advantageous for extracting information from signals that cannot be unraveled using a Fourier or even a windowed Fourier transforms [18,19]. It is rapidly becoming a typical technique for "zooming in" on transient high-frequency phenomena such as signal discontinuities and transient structures, as it enables the decomposition of data, functions, or operators into distinct frequency or scale components [20–23].

The mechanisms behind the formation of an earthquake at the most recent stage of a seismic cycle have long attracted scientists' attention and sparked controversy. Seismicity is one consequence of dynamic processes occurring in Earth's lithosphere [24], and approaches to earthquake prediction are based on processes that precede seismic ruptures [25–27]. A significant number of works study ionospheric perturbations that occur prior to large earthquakes [25,28–32]. The lithosphere-ionosphere coupling (LIC) mechanism is based on the relation between ionospheric anomalies and earthquake occurrences, which are well proven to exist [24,33,34]. On these works, it is well proven the existence of an abnormal ionosphere behavior before [26,33,35,36] and after [37] seismic activity. Most of the existing LIC models believe that large-scale currents flow over a future fault and induce electromagnetic field variations that are propagated into the ionosphere (e.g., [38]). However, these models encounter significant challenges to explain the attenuation of electric fields as a result of the rapid increased ionization with altitude. Similarly, [39] suggested that atmospheric stratification amplifies the signals. [24] later proposed the existence of sufficiently intense sources of low-frequency disturbances which could result in the formation of internal gravity waves (IGWs). In this scheme, the observed ionospheric perturbations could be caused by IGW dissipation with altitude [40]. However, no clear evidences of pre-seismic long-period ground-based oscillations have been found, even with highly sensitive superconducting gravimeters. Other studies claim a pre-seismic temperature increase in Earth's surface as latent heat flux and infrared radiation, which is difficult to relate to ionosphere anomalies [41]. Furthermore, due to the high permeability of fault zones in seismically active regions, lithosphere gas outflow is regarded as the most noticeable aspect of geophysical activity prior to earthquakes [42]. It is believed the high permeability of the fault zones increases the gas outflow from the lithospheric subsurface into the atmosphere. It has been suggested that lithosphere gas discharges are dense, increasing by orders of magnitude prior to seismic activity, resulting in anomalous CO<sub>2</sub> and CH<sub>4</sub> emanation [42]. However, the LIC mechanism can clarify the energy transmission from underground to the atmosphere [27,43]. To date, the role of the global electric circuit is elucidated with a deeper understanding of LIC [44]. Notwithstanding, the process of identifying precursors to earthquakes is becoming increasingly sophisticated, and physically grounded; each seismic event is different, and the close similarity of precursors for different earthquakes is an inherent property of the LAIC, which features may be employed for automatic detection [32].

On the other side, in order to understand the dynamics of ionosphere, especially during geomagnetic storms, we must first understand how the disrupted solar wind plasma reaches the Earth's ionosphere. Basically, the solar wind is embedded in the interplanetary magnetic field (IMF) and it electromagnetically interacts with the Earth's magnetic field, releasing a significant amount of energy into the terrestrial environment [45–48]. The magnetosphere becomes extremely perturbed if this state endures for several hours [49,50]. Usually, existing magnetospheric and ionospheric quiet currents are expanded and amplified due to an increased coupling between the solar-wind and the Earth's magnetosphere [51]. At medium and low latitudes, the ring current dominates, whereas at higher latitudes, a system of ionospheric electrojet currents running horizontally in the auroral oval prevail. These currents characterize geomagnetic storms and geomagnetic sub storms [52,53]. Another current system, names field-aligned currents (FACs), connects the high and low latitude current systems and enhances complexity [54]. All these currents particularly affect the horizontal component of the Earth's geomagnetic field, which is employed for the calculation of the disturbance storm time (Dst) index, useful to represent variations in the equatorial ring current [55,56]. On the other side, the Auroral Electrojet (AE) index describes the perturbations in the auroral electrojet current system [57], as its name indicates. According to [58], normal fluctuations of geomagnetic field measurements are on the order of 0.1 - 10 mHz (periods 1.66 min - 2.77 hours), while fluctuations of geomagnetic data can show a complex structure of irregularities and multifractal features due to large microstructural noise such as low-frequency plasma instability [58]. As a result, effective extraction of information conveyed at multiple frequencies can provide a successful mining data set. Bayer et al. [59] and the references therein describe several applications to study geomagnetic data using the WT approach, where fluctuations were detect in the horizontal component of the geomagnetic field. The WT enables viewing shocks (singularities) in geomagnetic data derived from magnetograms acquired at different sites.

This paper investigates the application of WT for singularity detection of associated discontinuities in geomagnetic data and coupling mechanisms to seismic data. We first introduce a conceptual definition of the WT and then consider various applications linked to seismic and geomagnetic phenomena. We also show how magnetogram data, rather than the processed Dst index, can be used to identify quiescent and non-quiescent periods during geomagnetic storms. The next section presents the data and methods used in this study. Finally, Section 3 shows and describes the results obtained, and last section provides our conclusions based on the achieved results and their contrast to previous works.

## 2. Data and Methods

### 2.1. Data

Ground-based seismic data recorded at the Darcena Station in Chile is provided at <https://www.strongmotioncenter.org/>. Space weather data is provided at the NASA Omniweb powtal ([https://omniweb.gsfc.nasa.gov/form/omni\\_min.html](https://omniweb.gsfc.nasa.gov/form/omni_min.html)). The data used in this work include solar wind parameters (Plasma Temperature, Velocity of solar wind, proton density), magnitude of interplanetary magnetic field and its Cartesian components, and several geomagnetic indices, including the AE and the SYM-H indices. The SYM-H index is provided at 1 min resolution and it is used to identify the phases of a geomagnetic storm.

### 2.2. Methods

Several mathematical tools have been developed to study signals. The Fourier Transformation (FT) deals with the frequency content, while it provides no information regarding the epoch when the peaks appear. Thus, FT provides spectral information but is not suitable to fully study the characteristics of non-stationary signals. In order to overcome this problem, Gabor introduced a Gaussian window Fourier transformation. The window is of fixed width, localized in time, so that the data can be explored at a different epochs. However, this approach doesn't give a proper resolution in both epoch versus frequency, simultaneously, due to the limitations of using a fixed window's width. The struggle appears in selection of the window as it exists an inverse relation between window length and frequency bandwidth. In one hand, a narrow window would provide a good time resolution

but a poor frequency resolution, and in the other hand, a wider window would give good frequency resolution but poor time resolution. Fortunately, the wavelet transform can solve this problems by providing a multi-resolution analysis in time and frequency domain. This approach has the ability to work with a dynamic window; a window will be narrowed automatically to observe the high frequency content and it will be widened to capture the high frequency content in the data. During the analysis, the mother wavelet is decomposed into series of basis functions containing dilated and translated mother wavelet function.

The continuous wavelet transform (CWT) is an integral transform that decomposes a signal in terms of special functions called wavelets, that are well-localized waves in both time and frequency domains. In other terms, given a signal  $f$  with finite energy, the CWT of  $f$  in an instant of time  $b$  and scale  $a > 0$  is defined by

$$Wf(a, b) = \int_{-\infty}^{+\infty} f(t) \psi_{a,b}^*(t) dt \quad (4)$$

where  $\psi_{a,b}^*$  denotes the complex conjugate of

$$\psi_{a,b}(t) = \frac{1}{\sqrt{a}} \psi\left(\frac{t-b}{a}\right) \quad (5)$$

Equation (4) represents a family of wavelets that are scaled and translated versions of the mother wavelet  $\psi$ , which is chosen according to the application. The variables  $a$  and  $b$  are called time and scale parameters, respectively. The time parameter essentially translates the wavelet along the signal, whereas the scaling parameter controls the compression or dilation state or filter bandwidth of the wavelet. If  $a > 1$ , then  $\psi_{a,b}$  is in a dilated state resulting in a wide analyzing function or a low pass filter, whereas if  $a < 1$ , then it is in a compressed state resulting in a narrow analyzing function or a high pass filter.

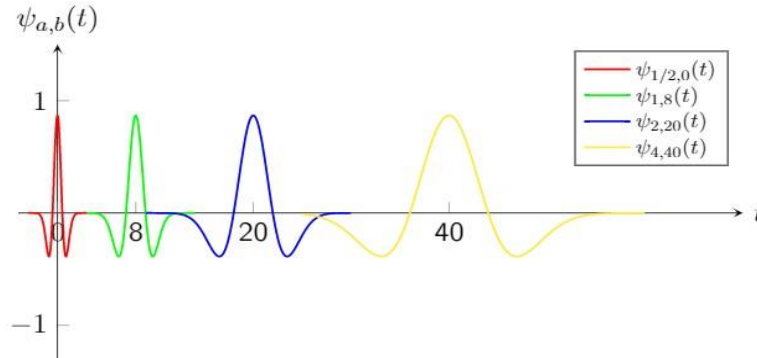


**Figure 1.** Some of the daughter wavelets associated to the Marr wavelet.

Two popular wavelet functions for CWT are Mexican Hat and Morlet Wavelet. The Mexican wavelet [see figure 2 (left)] is defined as the second derivative of the Gaussian Function, given as,

$$\Psi(t) = \frac{2}{\sqrt{3}} \pi^{-\frac{1}{4}} (1 - t^2) e^{-\frac{t^2}{2}}$$

There are different forms to express the Morlet wavelet. For our work we are considering the complex Morlet wavelet [see figure 2(right)] given as

$$\Psi(t) = \pi^{-\frac{1}{4}} e^{-i\omega_0 t} e^{-\frac{t^2}{2}}$$

On the other hand, the inverse wavelet transform ICWT is defined by

$$f(t) = \frac{1}{C_\psi} \int_0^{+\infty} \int_{-\infty}^{+\infty} Wf(a, b) \psi_{a,b}(t) \frac{da}{a^2} db \quad (6)$$

where  $C_\psi$  is the admissibility constant, that depends on the choice of the mother wavelet  $\psi$ , and is given by

$$C_\psi = \int_{-\infty}^{+\infty} \frac{|\psi(\omega)|^2}{\omega} d\omega \quad (7)$$

Note that equation (6) represents a synthesis equation since it reconstructs the original function  $f$  as a linear combination of translated and scaled versions of the mother wavelet, whose coefficients comes from equation (4). As one can notice in equation (7),  $C_\psi$  must be finite so that reconstruction is possible. This condition is called admissibility condition. Scalogram is the visual display of the wavelet transform. Scalogram is obtained by taking the square modulus of the wavelet coefficients of CWT. A wavelet transform is the energy preserving transformation and thus we can write

$$\int_{-\infty}^{+\infty} |x(t)|^2 dt = \frac{1}{C_\Psi} \int_{-\infty}^{+\infty} \int_0^{+\infty} \frac{1}{s^2} |W(\tau, s)|^2 d\tau ds$$

Then the function  $|W(\tau, s)|^2$  is called scalogram. However, if we take the product CWT of the two distinct function as,

$$\int_{-\infty}^{+\infty} f(t)g^*(t)dt = \frac{1}{C_\Psi} \int_0^{+\infty} \frac{1}{s^2} \int_{-\infty}^{+\infty} W_f^\Psi(\tau, s)W_g^{*\Psi}(\tau, s)d\tau ds$$

Then the product  $W_f^\Psi(\tau, s)W_g^{*\Psi}(\tau, s)$  is called cross scalogram or co-scalogram. A Scalogram reveals much more information about the characteristics of non-stationary signal that was previously hidden in the original signal. Scalogram can be observed in case both DWT and CWT. In the non-stationary process there is the transfer of energy between different frequency bands and Scalogram is the tool that helps to visualize how this transfer takes place. A cross scalogram or co-scalogram gives the interpretation about the interaction between two processes. The Scalogram is also able to visualize the multiscale feature i.e. large- or small-scale feature in the signal along with their location. Each scalogram is characterized by the cone of influence due to the edge effect of the signal. During WT, the analyzing window must be within the observation interval of the original signal, but in case if the analyzing window lies outside the signal then edge effects occur. The edge effect is seen at the beginning area and the end area of the sampled signal as placing the window function at beginning or end sampled points will result that some part of it doesn't lying within the observation interval. In such condition, analyzing window may consider the left out portion of signal to be zero, thus leading to the production of artifacts in CWT. Therefore, during the signals analysis, the scalogram value with in cone of influence is considered. One way of coming out of this problem is zero padding at the end of the time series and then removing it afterwards.

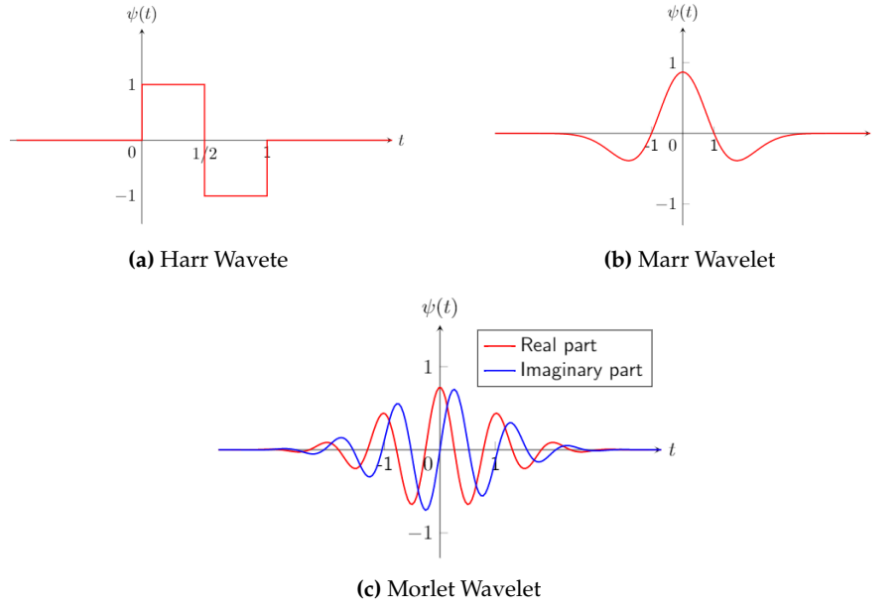


**Figure 2.** Representation of the waveforms of some wavelets that appear frequently in the specialized literature.

On the other side, the Discrete Wavelet Transform (DWT) is a linear multilevel efficient transform which operates usually on a data vector whose length is an integral power of two. This transformation is very popular in data compression methodologies due to its fast algorithm and good local representation in multilevel. DWT may or may not have the redundant representation depending upon the discrete scheme used. In DWT we choose the scales in the form of power ( $s = 2^m$ ) and translational parameter proportional to the scale ( $\tau = n2^m$ ) then the DWT coefficient is defined as,

$$T(m, n) = \int_{-\infty}^{+\infty} x(t) \Psi_{m,n}(t) dt \quad (8)$$

Where  $\Psi_{m,n}$  is obtained as  $\Psi_{(m,n)}(t) = 2^{-\frac{m}{2}} \Psi_0(2^{-m}t - n)$ .

The main reason of dyadic scale is to form orthonormal basis which avoids the redundancies in the signal. DWT is all about approximation and details. It ensures how well a signal can be approximated on moving from one level to the next. The DWT coefficients evaluated at scale  $2^m$  or level  $m$  capture the “details” in the signal  $x(t)$  at that particular scale. The scale refers to the resolution in DWT which is analogous to the understanding of frequency band in CWT. Thus, as the scale is increasing, we move further towards the coarser resolution and as the scale is decreased we move toward the finer resolution.

The DWT coefficients at the certain level  $m$  are spaced  $2^m T_s$  apart, with  $T_s$  being the sampling time or sampling interval. In such case on increasing scale we lose out the time resolution. For example, if we move from  $s=1$  to  $s=2$  or  $m=0$  to  $m=1$  then sampling time falls off by the factor of 2 and at  $m=2$  it falls off by the factor of 4. This implies to obtain the better frequency resolution we lose time resolution. One of the important things to notice here are that the coefficients at level  $m$  contains the details that are necessary to construct approximation at finer level  $m-1$  from the approximation level at  $m$ .

A tool known as multi-Resolution (MR) analysis is used to construct the wavelet functions that are used in the DWT. Let's define the MR analysis and its basic properties. A multiresolution analysis of the space  $L^2(\mathbb{R})$  is a sequence of subspaces  $\{V_m \mid m \in \mathbb{Z}, V_m \in L^2(\mathbb{R})\}$  obeying following conditions:

$$\dots V_{-1} \subset V_0 \subset V_1 \subset \dots$$

$$\bigcup_{m=-\infty}^{\infty} V_m = L^2(\mathbb{R})$$

$$\bigcap_{m=-\infty}^{\infty} V_m = \{0\}$$

$$f(x) \in V_m \Leftrightarrow f(2x) \in V_{m+1} \quad (9)$$

$$f(x) \in V_0 \Leftrightarrow f(x-k) \in V_0, k \in \mathbb{Z}$$

There exists a function  $\Phi \in V_0$  such that the set  $\{\Phi_{0,n} = \Phi(x-k); k \in \mathbb{Z}\}$  forms Riesz basis for  $V_0$ . Based on this relation we can find a scalar relation,

$$\frac{1}{\sqrt{2}}\Phi\left(\frac{t}{2}\right) = \sum h[n]\Phi(t-n)$$

Where

$$h[n] = \left\langle \frac{1}{\sqrt{2}}\Phi\left(\frac{t}{2}\right) \mid \Phi(t-n) \right\rangle$$

Here  $\Phi(t)$  is the scaling function and  $h[n]$  is coefficients of scaling factor. In the relation we see that  $h[n]$  is convolute with  $\Phi(t)$  producing dilated wavelet. This concludes, apart from performing the convolution we are down sampling the signal by the factor of 2. Thus  $h[n]$  is called to be low pass filters. So low pass filters along with scaling functions helps us to move from finer to coarser approximation.

The first requirement shows the subspaces are nested. As we move from  $V_0$  to  $V_1$  we are moving to the coarser scale so we are missing out some information and we this information "details" of the signal at that level. These details are contained in another subspace denote as  $W_1$ . Moving further coarser with increasing scale at each time we will have such details contained in such sub spaces which are mutually exclusive. And these details are nothing but the projection of signal  $f(t)$  into the wavelet function rather than scaling function. If we denote the spaces spanned by the wavelets, then following the theory of MRA we arrive at the conclusion

$$V_{m-1} = V_m \oplus W_m$$

We know  $W_m \subset V_{m-1}$  thus we arrive at the relation that,

$$\frac{1}{\sqrt{2}}\Psi\left(\frac{t}{2}\right) = \sum g[n]\Phi(t-n),$$

where

$$g[n] = \left\langle \frac{1}{\sqrt{2}}\Phi\left(\frac{t}{2}\right) \mid \Phi(t-n) \right\rangle$$

This expression shows that the function in  $W$  subspace can be expressed as the linear combination of the basis function of sub space  $V$  and the basis of  $V$  are scaling function.

The coefficients  $g[n]$  are complementary to  $h[n]$  and thus called to be high pass filter because these coefficients help to capture details not the approximations. The relation between high pass filter and low pass filter is given as;

$$g[n] = (-1)^{1-n}h[n]$$

As summary, first of the entire low pass filter  $h[n]$  is specified and high pass filter  $g[n]$  is computed. With high and low pass filter we determine the scale functions and then the wavelet function and then finally we can obtain the projections onto sub-space  $V_m$  and  $W_m$  to obtain the approximations and details. One of the results of such construction is Daubechies orthogonal wavelet function (see figure 3). Those functions don't have the mathematical expression and are not symmetrical. In the figure the wavelets of order 2, 3, 4 and 5 are shown which are denoted as db2, db3, db4 and db5 respectively.

The Daubechies wavelet function of order two is chosen in this work because it can detect the first order local disturbances in the signal and its derivatives. As they form an orthogonal system no redundant information is stored within the wavelet coefficient.

One property used here is that, in the wavelet domain of smooth data few localized structure many wavelet coefficients with small amplitude can be neglected, and one still has a good representation of the data. Therefore, in these cases, we have a compact representation of the data, and moreover we can identify the disturbed regions on the data just by looking at the amplitudes of the wavelet coefficients.

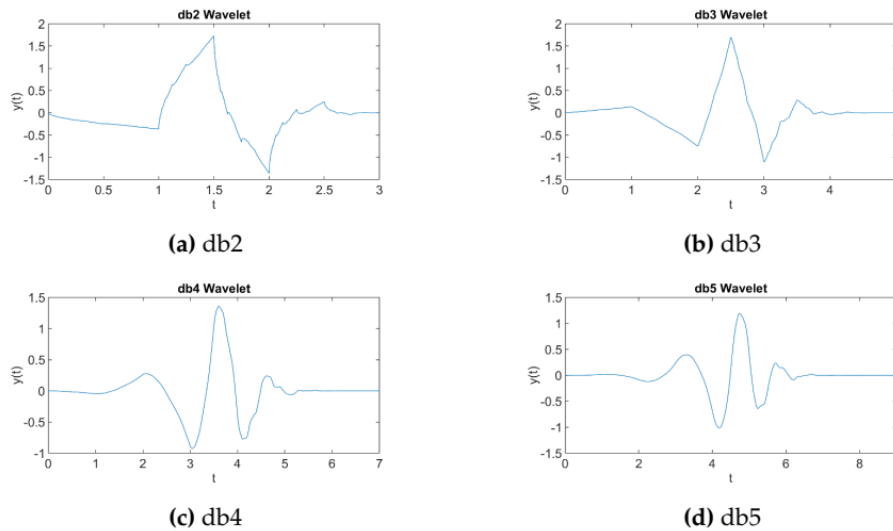


**Figure 3.** Wavelet Family Daubechies (db).

### 3. Results

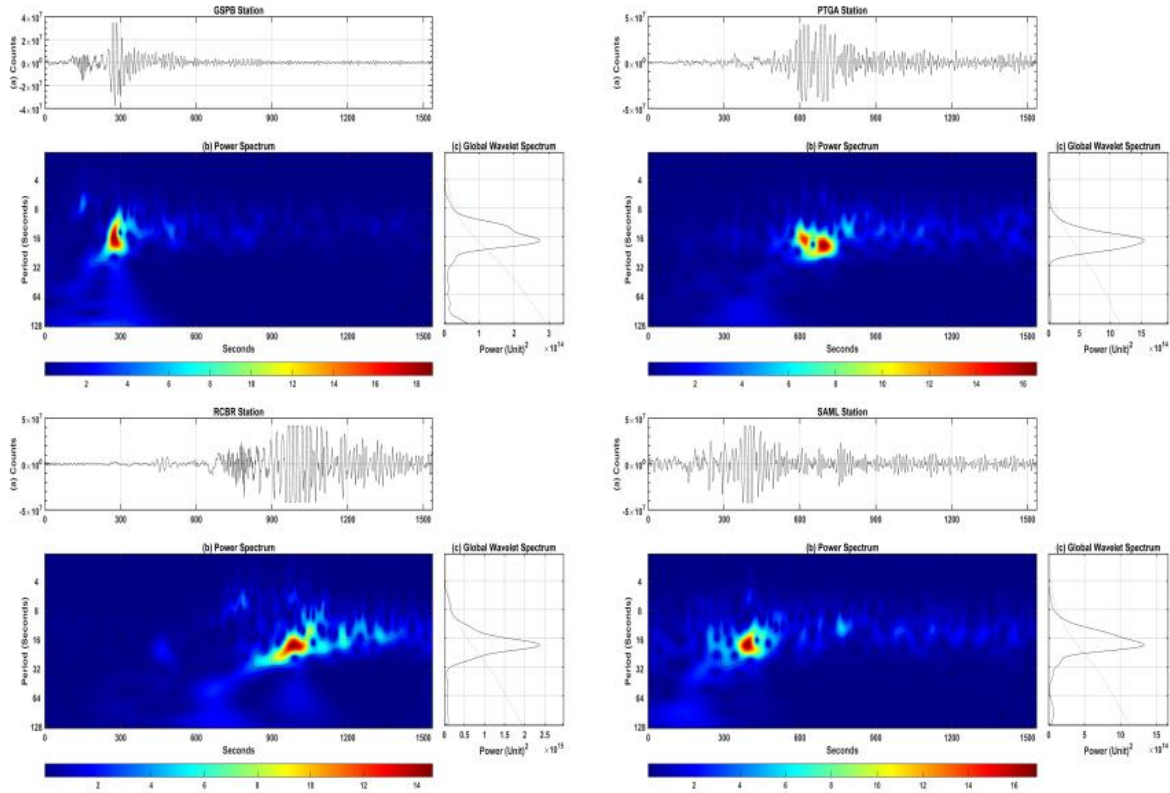
#### 3.1. Seismograms

Figure 4 displays the result of CWT to seismic acceleration data. The wavelet power spectra were analyzed using the *Morlet* wavelet normalized for spectral analysis of counts by  $\sigma^{-2}$ , where  $\sigma$  is the variance [60]. The power spectrum include regions with a 95% confidence level (significance level of 5%), under the red noise processing level [60]. The red noise processing level concerns the construction of a background spectrum employed to shape a null hypothesis for the power regions observed in the wavelet spectra [46]. The construction of a red noise requires the selection of an appropriate lag 1 autocorrelation coefficient



(the correlation between values that are one time period apart), which is set to 0.72. This analysis helps to understand the patterns relative to seismic events that occurred on 16 September 2015 at 22:54 UT. These figures display the time-frequency sketch of counts recorded by GSPB, PTGA, RCBR, and SAML stations, respectively. In these figures, the x-axis is the time in seconds from 23:00 UT to 23:30 UT on 16 September 2015, and the y-axis is the wavelet spectrum as a function of period. Several particular aspects can be examined, for example, it is possible to depict the energy distribution of signals in both frequency and time.

The enhancements of amplitude with discontinuities that occur in the signal, and then to observe the abrupt changes in the data. The count time-series is padded with appropriate zeros to get the data size equal to  $2N$  for the wavelet processing. This method of adding zeros, however, creates discontinuities at the edges of the time series, which is solved by inserting a cone of influence (represented in the figures with U-shaped black lines). Anything underneath the cone of influence becomes trivial and can be ignored in the study [61]. The peaks observed in the plot show the main periodicities during the event.



**Figure 4.** Acceleration data analysis during the seismic event on 16 September 2015. The scalogram and the global wavelet spectrum of counts are shown for the different stations used in this study. The x-axis is the time in seconds from 23:00 UT to 23:30 UT on 16 September 2015. The stations are shown in the map of Figure 8.

From Figure 4, in case of GSPB station, enhanced counts are clustered around the period of 10-25 s (0.1-0.04 Hz) at 23:05 UTC. The corresponding global wavelet spectrums provides a main periodicity of  $\sim 18$  s with an energy of  $2.7 \times 10^{14}$  unit<sup>2</sup>. For the PTGA station, the power region corresponding to counts exists between the period of 32-16 s (0.03125-0.0625 Hz) and the global wavelet spectrum provides again a main periodicity of  $\sim 18$  s with an energy of  $1.5 \times 10^{15}$  unit<sup>2</sup>. Concerning the RCBR station, it is evident that the observed count is enhanced with the most significant periodicity of 32-16 s (0.03125-0.0625 Hz) at 23:16 UTC. On the other hand, long-term count intensification is observed to extend after 23:20 with key periodicities between 18 and 8 s. We found high wavelet power corresponding to 18 s with energy  $2.4 \times$

$10^{15} \text{ unit}^2$ . Similarly to GSPB, the SAML station intensifies at 23:05 UTC with periodicities between 8 and 24 s, with a maximum of energy  $1.3 \times 10^{15} \text{ unit}^2$  at 18 s.

We conducted a wavelet transformation of the count-time series in all the stations chosen for this analysis in the statistical study of periodicity in the counts during the seismic event. By manually examining the count power spectrum of each case, the counts are found to exhibit a typical periodicity of 18 s. The variations in the count, however, differ with time, depending on the distance from the epicenter, local time, etc. We may assume that any building with or close to this frequency band with natural frequencies has a high likelihood of resonance and destruction [17]. Therefore, we noticed that CWT is a strong method for understanding the nature of seismic waves.

Furthermore, the DWT is used to measure the effectiveness of the wavelet coefficients at 3 levels of decomposition. In this way, for each station, it is possible to detect the local quiet and disturbed periods. The variations in counts correlated with seismic events on 16 September 2015 will be evaluated in this work, based upon the works by [45,62–66]. As discussed in [65], the coefficient of the wavelet can be called a local error of approximation. In addition, wavelet coefficients can be used as local signal regularity markers. The local approximation error depends on the choice of analyzing wavelet function, and thus the wavelet coefficients will indicate the local error achieved by this approximation. These local errors often detect the local regularity of the high-order signal derivatives. Normally, a visual inspection cannot perceive this type of feature.

Figure 5 shows the squared wavelet coefficients for DWT related to integer count during the seismic event of 16 September 2015 for the stations used in this study. The uppermost panel for each station represents the count, and the lower 3 panels show the amplitude of squared wavelet coefficients at 3 decomposition levels (d1, d2, and d3).

The use of the Daubechies wavelet coefficient amplitude relies on the fact that it represents the local regularity present in the signal [10,45,67]. This allows us to detect first-order local disturbances in the signal and its derivatives [68]. As a property of the wavelet analysis, it is possible to show that the amplitude of the square wavelet coefficient is the local indicators of signals [69–72].

In Figure 5, the first level of decomposition is in association with the mainshock of the earthquake. The abrupt variation of the counts corresponds to a different time periods, which are observed at 350-400 sec, 800-1050 s, 600-800 s, and 100-400 s at SAML, RCBR, PTGA, and GSPB, respectively. The sudden variations in the counts are emphasized by the highest amplitudes of the wavelet coefficients. The seismic activities are well identified by the first and second levels of decomposition. The third level of decomposition presents the highest wavelet coefficients amplitudes associated with the event at SAML and PTGA station.

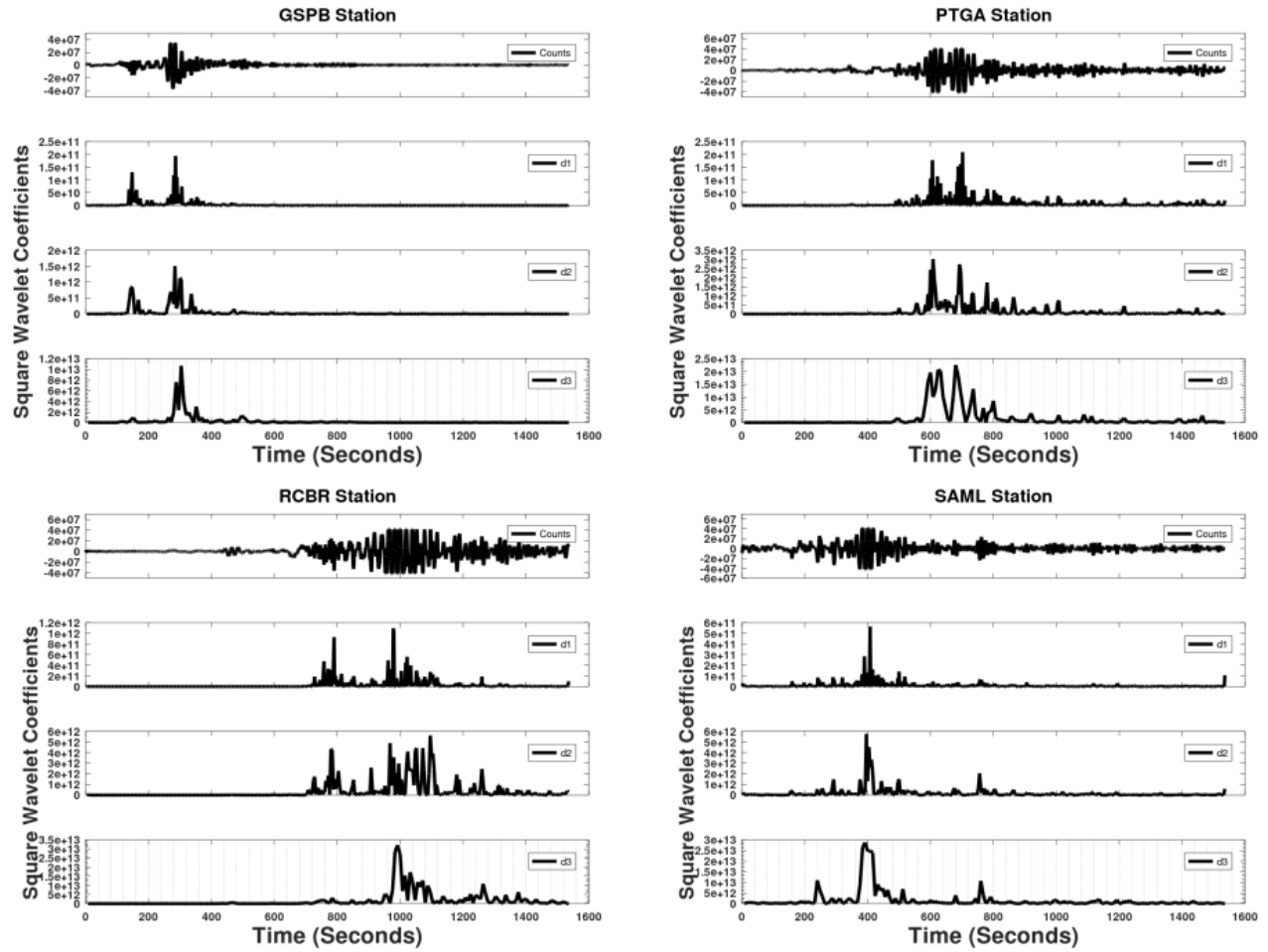


**Figure 5.** Wavelet coefficients from  $j=1$  to  $j=3$  during the period 23:00:00 to 23:30:35 UT on 16 September 2015 for the stations used in this study.

The findings obtained show the counts during the seismic event are well localized by all three decomposition levels. The wavelet method for the identification of singularities is to represent abrupt variations or to detect different steps in seismic times-series.

### 3.2. Geomagnetic and Ionospheric data

Figures 6 and 7 show the H- and Z-components during September 16–17, 2015, respectively. Each top panel shows the mean value (black line) of the five quietest day of September (2015) and the standard deviation (gray lines) in relation to the mean value. The day of September 16, 2015 is highlighted in blue color. The bottom panel indicates an enlarged view of the dashed box region shown in the top panel. A presence of a magnetic pulse around 23:25 UT, about  $\sim 30$  min after the main shock is noticed on night of the Illapel earthquake in both H- and Z-components for each Brazilian magnetic observatories. Such pulse is not present in any other quiet day of September, 2015.

Motivated by the previous studies of seismogenic and tsunamigenic disturbances, we search for ionospheric disturbances in the present study due to the Chilean earthquake (2015). We select a Brazilian observatory located at São José dos Campos (SJC -  $23.2^\circ$  S,  $45.9^\circ$  W) and present the observations from the all-sky imager. This all-sky imager is a  $180^\circ$  field of view multispectral imaging system that uses four 4-inch diameter interference filter of 2.0 nm bandwidth for OI 557.7 nm emission. The OI 557.7-nm greenline emission has

been largely used to investigate wave dynamical processes around the mesopause region. In this kind of images, it is possible to observe gravity waves and tides signatures as well as infer the atomic oxygen profile [73]. The OI 557.7-nm emission volumetric peak rate occurs around  $95 \pm 2$  km. In Figure 8, the epicenter of earthquake and SJC observatory location are shown. Also, it is shown an airglow image over SJC with effective field of view. In Figures 9 and 10, we present the images on the night of September 16–17, 2015 obtained from all-sky imager. Figure 9 shows sequences of the OI 557.7-nm emission images. In these images, we note the presence of faint band-like airglow disturbances that appear around 02:05 UT (3 hours and 5 minutes after the earthquake event) and last about 30 minutes. These airglow disturbances have wavefront aligned in northwest-southeast and propagated in northeastward direction, *i.e.*, in the opposite direction to the tsunami propagation. From an enlarged image at 02:05 UT in Figure 10, we note that these disturbances have wavelength in between 60 to 100 km. We verify that such disturbances as noted on the night of tsunami are absent on the days before and after the earthquake.

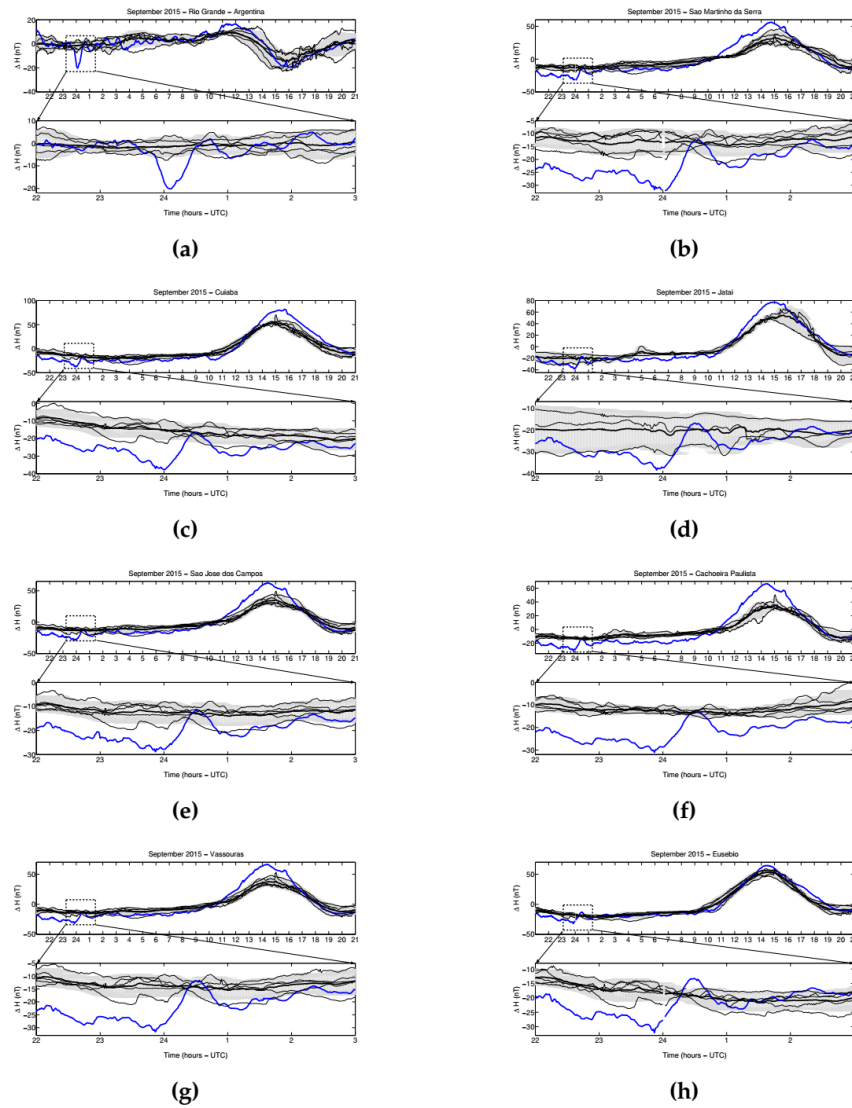


**Figure 6.** Minutely H-component data for five quietest days of September, 2015 (black thin lines) according to GFZ. From top to bottom, each panel shows the H-component and Z-component variations. The black thick line corresponds to mean value variation of these all five quietest days and the blue color line corresponds to the day of 16/17th September, 2015. On top panel, the horizontal axis varies from 21:01 UT (16, Sep. 2015) until 21:00 UT (24 h period).

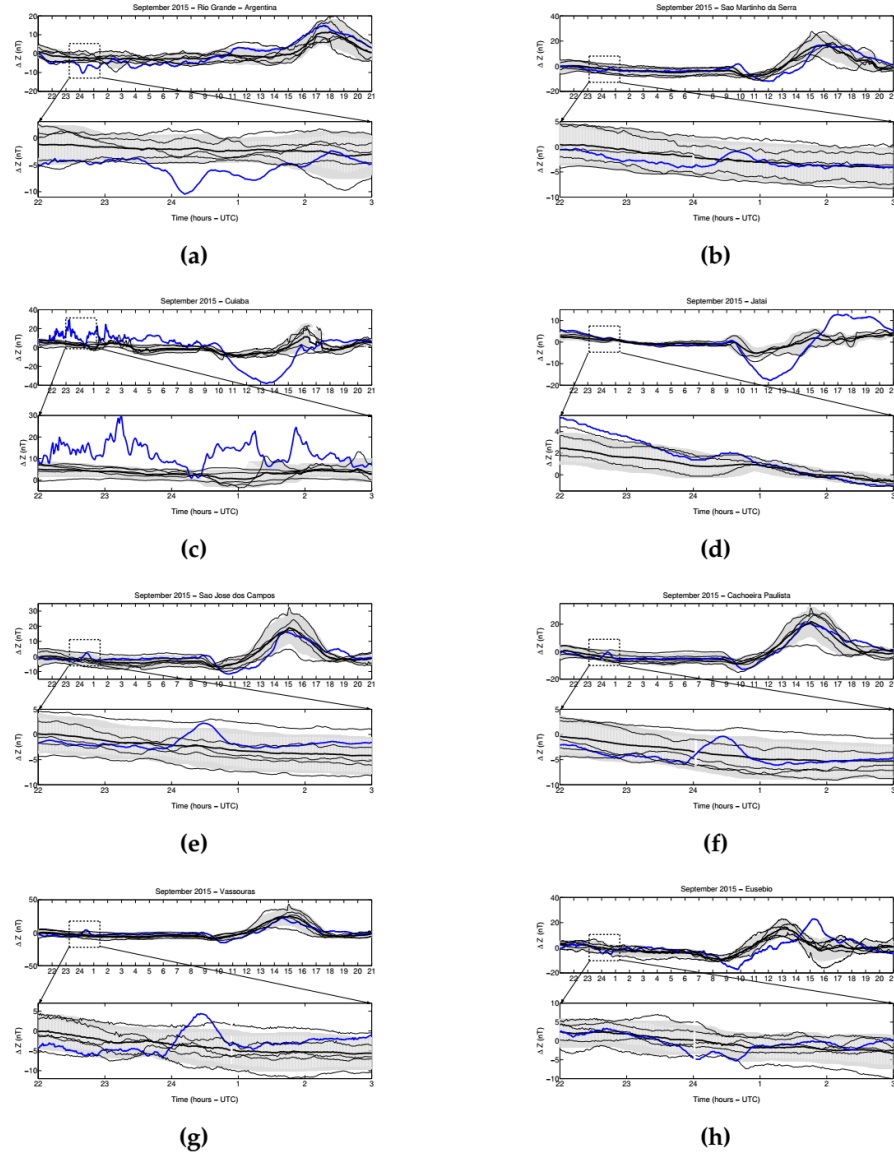


**Figure 7.** Minutely Z-component data for five quietest days of September, 2015 (black thin lines) according to GFZ. From top to bottom, each panel shows the H-component and Z-component variations. The black thick line corresponds to mean value variation of these all five quietest days and the blue color line corresponds to the day of 16/17th September, 2015. On the horizontal axis, the time varies from 11:00 UT (16, Sep. 2015) until 10:59 UT (24 h period).

Band-like airglow disturbances are common feature over Brazilian region, and they are associated to gravity waves/medium-scale traveling ionospheric disturbances (GWs/MSTIDs) [74–77]. Both mesospheric GWs and MSTIDs signatures observed in airglow images by [74–77] are commonly attributed to tropospheric convective processes or to middle latitude instabilities. In addition, they have opposite orientation (northeast to southwest) and propagation direction (northwestward) to those observed here. Therefore, the observed airglow disturbances in Figures 9 and 10 are not the convectively-driven GWs/MSTIDs commonly observed in the region.

These disturbances are possibly seismogenic. These airglow disturbances observed over São José dos Campos may be explained due to the arrival of Rayleigh waves in the region. The LAI coupling generates

gravity waves which propagate obliquely upward with vertical velocity of  $\sim 50$  m/s reaching thermospheric height after a few hours.

As simulated by [78], the structure of the atmosphere induces a strong acceleration and deceleration in the vertical and horizontal gravity wave propagation. The vertical velocity can vary in the order of  $\sim 30$  to  $110$  m/s which results in a theoretical time delay to reach the ionospheric height (300 km) over 120 minutes. The airglow disturbances observed here appear after two hours from the local atmosphere shaking and they can be interpreted as owing to the Rayleigh wave arrival and the LAI coupling. The presence of airglow disturbances are also expected in a few minutes from the Rayleigh wave arrival in the region as it was observed in the geomagnetic field based in the same LAI mechanism. However, during this period of time (following the local sunset) the all-sky imager was not operating and there are no data available.

It is equally possible that these disturbances also have contribution from tsunamigenic coupling. For the Tohoku-Oki tsunami, ionospheric disturbances in TEC were reported to propagate towards backward direction in the form of concentric wavefronts, and to arrive up to  $23^\circ$  from epicentral distance [79,80]. The airglow disturbances in Figures 9 and 10 offer a similar scenario where their presences are noted at 2000-3000 km ( $\sim 18^\circ - 27^\circ$ ) from epicentral distance in the backward direction. [81] compute a more complete scenario for tsunamigenic excited acoustic gravity waves. Considering a viscous dissipation term in both horizontal and vertical components, they explained a generation of secondary gravity waves, and these waves became dominate gravity waves. And probably, their radial propagation towards the continent is the disturbances observed in Figures 9 and 10. For the Tohoku-Oki tsunami, the backward propagating TEC disturbances were simulated and interpreted as owing to the strong atmosphere shaking from the tsunami forcing near the coast [81,82]. Therefore, the observed backward propagating airglow disturbances in the present study are possibly arising from the similar atmospheric shaking.

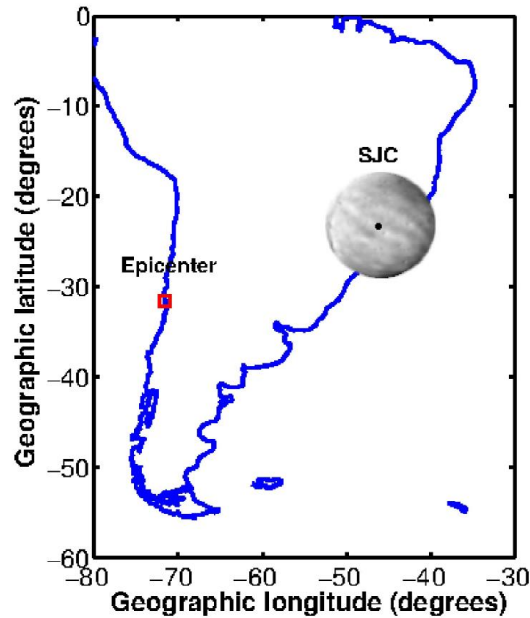


**Figure 8.** Locations of São José dos Campos observatory (SJC –  $23.2^\circ$  S,  $45.9^\circ$  W) used to geomagnetic field variations and airglow disturbances. The red square shows the epicenter of the Chilean earthquake of 16th September, 2015. The circle indicates the field of view at a zenith angle of  $90^\circ$  projected at a 100 km altitude and presents a raw image for OI 557.7-nm emission obtained at 23:05 LT over the field of view. The black dot shows SJC location.



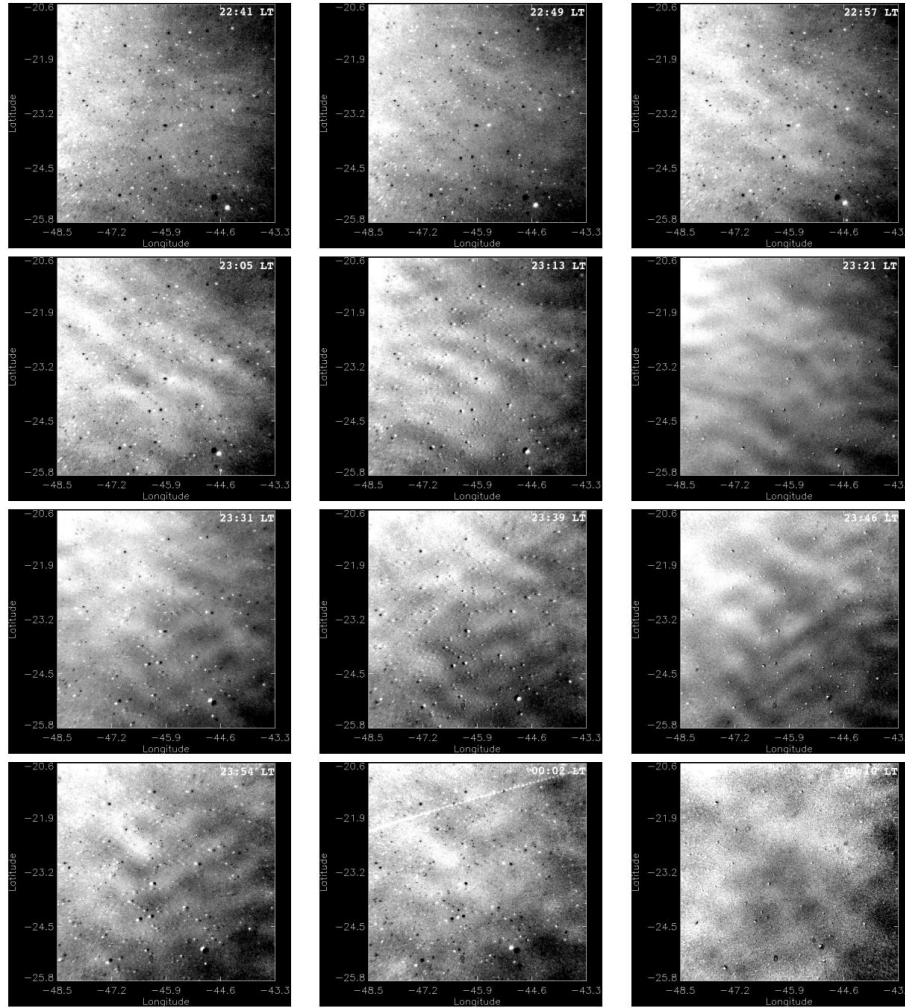


**Figure 9.** Sequence of the OI 557.7-nm emission all-sky images observed at “Universidade do Vale do Paraíba” (UNIVAP) at São José dos Campos (23.2° S, 45.9° W);, showing the time evolution (between 22:41 LT (01:41 UT) and 00:10 LT (03:10 UT)) and spatial characteristics of gravity wave propagation on the night of 16–17th September, 2015. The top of every imaging is located at the North geographic and left at the West geographic.

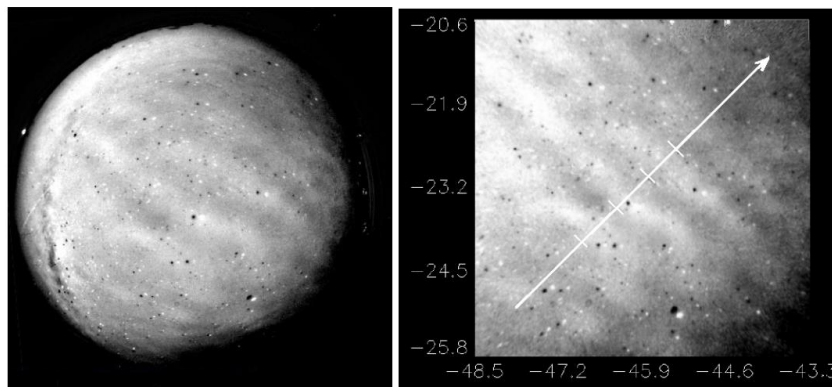


**Figure 10.** Airglow disturbance fronts propagating in Southeast direction. Vertical and horizontal axis are the latitude and longitude in degrees, respectively. The raw image at OI OI 557.7-nm at left and linearized at right obtained at 23:05 LT (02:05 UT).

### 3.3. Interplanetary data

Geomagnetic storms are characterized by fluctuations in the Earth's magnetic field caused by the injections of energetic particles in the Earth's magnetosphere. The major causes of the storms are high speed streams (co-rotating interaction region or CIR), magnetic clouds and interplanetary coronal mass ejections (ICMEs). During the main phase of storm, charged particles in the near-Earth plasma sheet are energized and injected deeper in to the magnetosphere. Thus, these energized particles cause large scale distribution in the magnetosphere and a large amount of energy is stored in the magnetotail and magnetosphere causing the ring current. The ring current in the magnetosphere produces diamagnetic effect. Magnetic storms are caused by mechanism of viscous interaction, predominantly by magnetic reconnection and resonant wave-particle interaction.

Among them the magnetic reconnection is the main and important mechanism. The storm time magnetic field variation produced by ring current is measured in Dst (disturb storm time) index.

In our work a CIR-driven geomagnetic storm has been chosen and the data includes the value of different solar parameters, IMF parameters and geomagnetic indices are shown in the Figure 11.

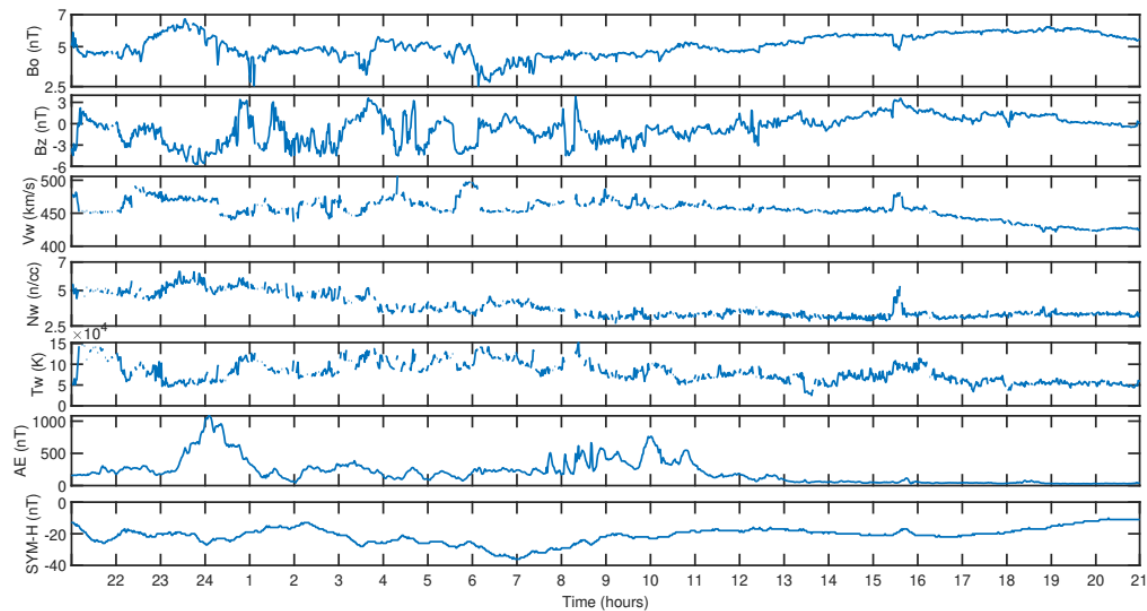


**Figure 11.** The interplanetary parameters on 16-17 September 2015. From top to bottom: field magnitude average -  $B_o$  (nT),  $B_z$  component (nT), solar wind speed -  $V_w$  (km/s), density -  $N_w$  (n/cc), solar wind temperature -  $T_w$  (K), AE index (nT), and SYM-H index (nT).



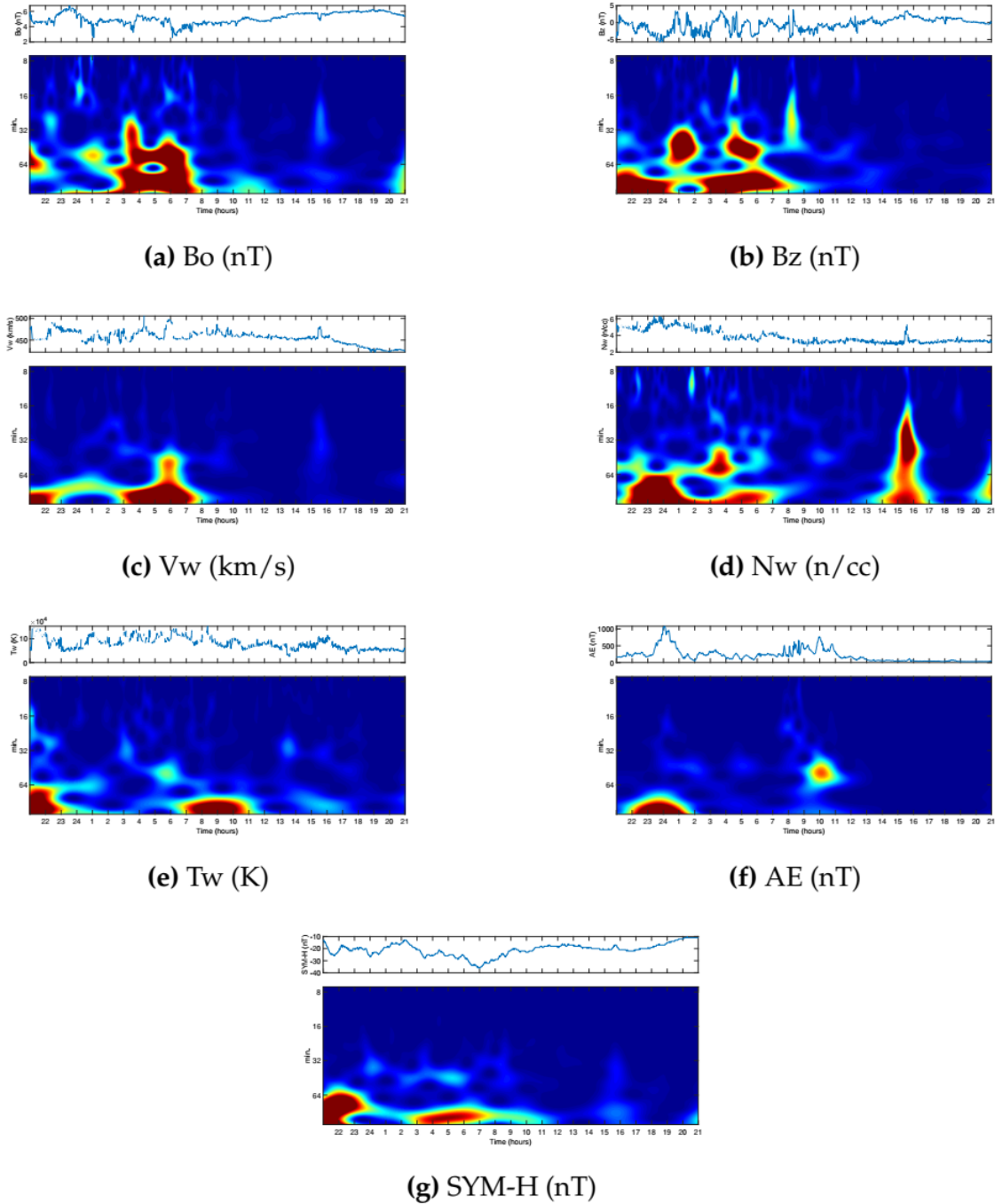


**Figure 12.** The interplanetary parameters on 16-17 september 2015 (top panel) and Wavelet Spectra (bottom panel).

Figure 11 shows the interplanetary event during 16 – 17 September 2015 and associated geomagnetic impacts. A substorm was detected during this period. A magnetic substorm means the disturbances caused in the Earth's magnetosphere when the interplanetary magnetic field turns southward. [52,83,85,86]. The IMF- $B_z$  directed southward, reaching a value of -6 nT at  $\sim 0$  UT. The southward directed  $B_z$  allows easy entrance for charged particles to the Earth's magnetosphere, which causes auroral activity [46,87]. As shown in figure 11, the flow speed ( $V_w$ ) shows a moderate speed stream up to 22 UT of 16 September 2015, and it suddenly peaked with a value of 480 km/s at  $\sim 22:30$  UT. Subsequently, a steady value was maintained and then increased to its second peak value of 500 km/s at 04:30 UT on 17 September 2015. The solar wind

temperature (Tw), plasma density (Nw), and magnitude of IMF (Bo) show the values of  $1.3 \times 10^5$  (K), 7 ( $\text{cm}^{-3}$ ), and 7 (nT), respectively. The SYM-H index shows depression at the main phase and shows the most negative value of  $\sim -35$  nT, then gradually rises within a few hours during the recovery phase. The AE index at the second last panel of this figure clearly shows the nature of the magnetic substorm, as indicated by the values around  $\sim 1000$  nT for almost an hour. During the recovery phase, the activity may diminish in the midnight sector, and the magnetosphere returns to its normal state.

Figure 12 depicts the scalogram of solar parameters, Bo, Bz, Vw, Nw, Tw and geomagnetic indices, AE and SYM-H during 16 September 2015 22 UT – 17 September 2015 23:59 UT, which is also the time-frequency analysis of the event. The signal energy in the wavelet space represented in the scalograms is visualized using a log2 function that highlights small perturbations [20,23,61,84,88]. The horizontal axis represents the time, *i.e.*, hours of the day, and the vertical axis represents the scales. The scale also corresponds to periodicity in minutes or the frequency band of the signal. The rectangular color bar represents the squared estimation of the time series data and is measured in  $(\text{unit})^2$ . In the scalogram, the area with the highest wavelet power is represented on top of the color bar, while the area with the lowest wavelet power is shown on the bottom.

From the scalogram, we see that there are dominant frequencies for Bo fluctuations, one in the period of 32-64 minutes and another one for 64-128 minutes. The power areas with peak intensity are seen around the regions (3 - 7 hrs). The scalogram also shows the occurrence of large- and small-scale feature at the same time. Similarly, the dominant frequencies for the geomagnetic indices, AE and SYM-H, occurred at the higher scale of periods of 64-128 minutes. The key periodicities of AE existed at two regions, one during 22 UT, 16 September to 1 UT, 17 September and the other at 10 UT of 17 September, whereas for SYM-H, one occurred at 22-23 UT of 16 September and the other at 3 - 7 UT of 17 September. The other remaining solar wind parameters, Bo, Vw, Nw and Tw shows variations with time without the presence of continuous periodicities. The wavelet power spectrum of Bz revealed dominant frequencies for its fluctuations at two different periods, one at 32-64 min in the regions 0-2 hrs and 4-6 hrs, other at 64-128 min in the regions 22 hrs (16 September) - 0 hr (17 September) and 3-7 hrs. Meanwhile, the flow speed (Vw) and plasma temperature (Tw) shows abrupt variation with a similar periodicity of 64-128 minutes in the region 3 – 7 hrs, and 7 – 10 hrs, respectively. Finally, the high-power regions in Nw Scalogram are observed at three dominant frequency regions, one at 16-64 min around 15-16 hrs, second at 32-64 min around 3-4 hrs and lastly at 64-128 minutes around the regions 22 (16 September) -6 hrs (17 September) and 15-16 hrs.

From the scalogram, we see that the less intense areas are approximately between the scales 8-16. This result shows that periodicity is showing continuity up to that scale. However, at the period or scale above 16 minutes, the periodicity is disturbed, and it is seen at higher scales that areas of the highest power have comparatively low periodicity. As the periodicity and the frequency have the inverse relation, the zone where the periodicity was found less are more frequent, and the zone where periodicity is high occurred less frequent. Thus, finding peak intensity with a high value at low periodicity strongly suggests these solar parameters can have variations more frequently during storm days. CWT has been revealed as a helpful tool for analyzing localized intermittent oscillations in a time series. The results show that the Morlet wavelet is a good choice for detecting different fluctuation periods of interplanetary parameters along with geomagnetic indices during the geomagnetic event. Our analysis also shows that the results obtained are encouraging because CWT well localizes the geomagnetic impacts associated with the interplanetary event by providing a time-frequency representation of the signal. *i.e.*, it helps to identify the geomagnetic storms and their global influence by analyzing the geomagnetic data.

#### 4. Conclusions

A signal can have a stationary or non-stationary nature and the mathematical tool require to analyze these signals are different. A Fourier analysis can be a tool to study a stationary signal as the power spectrum provides us with the perfect frequency localization. However, in case of the signal behaving non-stationary,

Fourier analysis is not the perfect tool. In contrast to the Fourier analysis the wavelet transform is best suited for such signals. As most of the phenomenon which occurs in the real world is non-stationary the use of wavelet transform has become inevitable. Wavelets provide a time frequency window which can provide us with the time and frequency localization of any kind of signal. This method offers us a window which shrinks for the high frequencies and widens for low frequencies, capturing the local behavior of the signal. In our work we have selected two physical phenomena i.e. Earthquake and Geomagnetic storm and applied both CWT and DWT to extract the information during this process. A CWT provides us with the time frequency analysis of any event with the help of scalogram.

This technique reveals where the energy is transferred and at what frequencies this occurs. This also shows how the low frequency component behaves during the whole event and how the high frequency component still having less periodicity can occur frequently. The scalogram also shows how both the high and low scales feature are embedded with each other at same time. A CWT analysis of the signal provides us with highly redundant information of the signal. Here we used Morlet wave to perform the CWT analysis of both events. In case of Chile Earthquake, we have seen that high-power high frequency component even with less periodicity is occurring throughout the quake and possibly this is the reason for bring the high destruction. A DWT based technique is used to obtain the non-redundant information of the signal. DWT is mainly used for discontinuity detection, signal compression, and signal estimation. It applies the method of thresholding to eliminate the coefficients. This type of method is used when we wish to see the abrupt changes and check the singularity in the signal. DWT along with the MRA helps in signal approximation of the signal. We can obtain approximations and details of the signal at different levels. In our work we used Daubechies wavelet and analyzed the coefficients up to three levels in each phenomenon. From the coefficients we were able to pick out the time where abrupt changes in signal occurred. The places where DWT coefficients have larger value are the place for sudden and abrupt variation in the signal. Thus DWT is used to detect high changes in the signal. Thus, we have shown how the wavelet transform can be used in non-stationary process. We found that the CWT enables us to find the frequency as well as time information about the signal and hence serves as a good tool for the time frequency analysis. The DWT wavelet coefficient helps us to identify the sudden variation and thus is a suitable tool to study the sudden variation and singularity in any non-stationary process. From our work we can infer that the application of wavelet transform is not limited and also it can be used to study in any desired interval of data.

#### **Author Contributions**

Binod Adhikari and Virginia Klausner developed the idea of this manuscript. They have major contribution to prepare introduction, dataset, methodology and conclusions. Humberto Gimenes Macedo has the major contribution on the methodology description and analysis. Pitamber Poudel has contribution on introduction and results. Ashok Silwal and Sujan Prasad Gautam has contributed on introduction, data plotting and description of application of WT to earthquake and geomagnetic storms. Andres Calabia contributed to revision tasks and supervision.

#### **Data Availability Statement**

N/A

#### **Acknowledgments**

The data used in case of Earthquake is the ground accelerations recorded at the Darcena Station, Chile which was downloaded from the website <https://www.strongmotioncenter.org/>. The solar wind parameters and geomagnetic indices are compiled from the website [https://omniweb.gsfc.nasa.gov/form/omni\\_min.html](https://omniweb.gsfc.nasa.gov/form/omni_min.html).

#### **Conflicts of Interest**

The authors declare that they have no competing interests.

#### **References**

1. Wang, B. & Wang, Y. Temporal structure of the Southern Oscillation as revealed by waveform <sup>588</sup> and wavelet analysis. *Journal of Climate* **1996**, 9(7), 1586-1598.
2. Nakken, M. & Wang, Y. Wavelet analysis of rainfall–runoff variability isolating climatic from anthropogenic patterns. *Environmental Modelling* **1999**, 14(4), 283-295.
3. Rathinasamy, M.; Agarwal, A.; Sivakumar, B.; Marwan, N.; Kurths, J. Wavelet analysis of pre<sup>592</sup> cipitation extremes over India and teleconnections to climate indices. *Stochastic Environmental <sup>593</sup> Research and Risk Assessment* **2019**, 33(11), 2053-2069.
4. Weng, H.; Lau, K. M. Wavelets, period doubling, and time–frequency localization with application to organization of convection over the tropical western Pacific. *Journal of Atmospheric Sciences* **1994**, 51(17), 2523-2541.
5. Farge, M. Wavelet transform and their applications to turbulence. *Annual Reviews of Fluid Mechanics* **1992**, 24, 395-457.
6. Bradshaw, G. A.; McIntosh, B. A. Detecting climate-induced patterns using wavelet analysis. *Environmental Pollution* **1994**, 83(1-2), 135-142.
7. Debret, M.; Sebag, D.; Crosta, X.; Massei, N.; Petit, J. R.; Chapron, E.; Bout-Roumazeilles, V. Evidence from wavelet analysis for a mid-Holocene transition in global climate forcing. *Quaternary Science Reviews* **2009**, 28(25-26), 2675-2688.
8. Yaghmaei-Sabegh, S. Detection of pulse-like ground motions based on continues wavelet transform. *Journal of seismology* **2010**, 14(4), 715-726.
9. Al-Hashmi, S.; Rawlins, A.; Vernon, F. A. *Wavelet Transform Method to Detect P and S-Phases in Three Component Seismic Data*, Scientific Research Publishing, 2013.
10. Mallat, S.G. Multiresolution approximations and wavelet orthonormal bases of  $l_2(\mathbb{R})$ . *Am. Math. Soc.* **1989**, 315(1), 69-87.
11. Rioul, O.; Vetterli, M. Wavelets and signal processing. *IEEE signal processing magazine* **1991**, 8(4), 14-38.
12. Meyer, Y. *Review of Books An introduction to wavelets by C. K. Chui, and Ten Lectures on Wavelets by I. Daubechies*. Bulletin (New Series) of the American Mathematical Society, 28(2), 350-360, 1993.
13. Daubechies, I. Review of the Books: Wavelets and Operators, Y. Meyer, (Cambridge University Press, New York, 1993). *Cambridge Studies in Advanced Mathematics* **1993**, 37.
14. Mallat, S. G. *A theory for multiresolution signal decomposition: the wavelet representation*. In *Fundamental Papers in Wavelet Theory* (pp. 494-513). Princeton University Press, 2009.
15. Mallat, S., *A Wavelet Tour of Signal Processing*. Academic Press, Burlington, 2009.
16. Sinha, S.; Routh, P. S.; Anno, P. D.; Castagna, J. P. Spectral decomposition of seismic data with continuous-wavelet transform. *Geophysics* **2005**, 70(6), P19-P25.
17. Adhikari, B.; Dahal, S.; Karki, M. et al. Application of wavelet for seismic wave analysis in Kathmandu Valley after the 2015 Gorkha earthquake, Nepal. *Geoenviron Disasters* **2020**, 7, 2, <https://doi.org/10.1186/s40677-019-0134-8>.
18. Klausner, V.; Almeida, T.; de Meneses, F. C.; Kherani, E. A.; Pillat, V. G.; and Muella, M. T. A. H. Chile2015: Induced magnetic fields on the Z-component by tsunami wave propagation. *Pure Appl. Geophys.* **2016b**, in press, doi:10.1007/s00024-016-1279-y.
19. Klausner, V.; Domingues, M. O. ; Mendes, O.; Mendes daCosta, A.; and Ojeda González, A. Latitudinal and longitudinal behavior of the geomagnetic field during a disturbed period: A case study using wavelet techniques. *Adv. Space Res.* **2016a**, in press, doi: 10.1016/j.asr.2016.01.018.
20. Strang, G.; Nguyen, T. Wavelet and filters bank, Wellesley-Cambridge, Cambridge, 1996.
21. Daubechies, I. Ten Lectures on Wavelets, Vol. 61 of CBMS-NSF Regional Conference (Series in Applied Mathematics), SIAM, Philadelphia, PA, 1992.
22. Ruskai, M. B.; Beylkin, G.; Coifman, R.; Daubechies, I.; Mallat, S.; Meyer, Y.; Raphael, L. Wavelets and their applications, Jones and Bartlett. Boston, Mass, 1992.
23. Foufoula-Georgiou, E., & Kumar, P. Wavelet analysis in geophysics: an introduction. In *Wavelet analysis and its applications*, Academic Press, Vol. 4, pp. 1-43, 1994.
24. Shalimov, S.; Gokhberg, M. Lithosphere–ionosphere coupling mechanism and its application to the earthquake in Iran on June 20, 1990, A review of ionospheric measurements and basic assumptions. *Physics of the Earth and Planetary Interiors* **1998**, 105(3-4), 211-218.
25. Pulinets, S. A.; Boyarchuk, K. A.; Hegai, V. V.; Karelin, A. V. Conception and model of seismo-ionosphere-magnetosphere coupling. *Seismo-Electromagnetics: Lithosphere-Atmosphere<sup>644</sup> Ionosphere Coupling* **2002**, 353-361.

26. Sharma, G.; Mohanty, S.; Kannaujiya, S. Ionospheric TEC modelling for earthquakes precursors from GPS data. *Quaternary International* **2017**, *462*, 65-74.
27. Pulnits, S.; Ouzounov, D.; Karelin, A.; Dmitry Davidenko, D. Lithosphere–atmosphere–ionosphere–magnetosphere coupling—a concept for pre-earthquake signals generation. *Pre-Earthquake Processes: A Multi-disciplinary Approach to Earthquake Prediction Studies*, 79-98, 2018.
28. Liu, J. Y.; Chen, Y. I.; Pulnits, S. A.; Tsai, Y. B.; Chuo, Y. J. Seismo-ionospheric signatures prior to  $M \geq 6.0$  Taiwan earthquakes. *Geophysical research letters* **2000**, *27(19)*, 3113-3116.
29. Molchanov, O.; Fedorov, E.; Schekotov, A.; Gordeev, E.; Chebrov, V et al. Lithosphere-atmosphere-ionosphere coupling as governing mechanism for preseismic short-term events in atmosphere and ionosphere. *Natural Hazards and Earth System Sciences* **2004**, *4(5/6)*, 757-767.
30. Pulnits, S. A.; Contreras, A. L.; Bisiacchi-Giraldi, G.; Ciraolo, L. Total electron content variations in the ionosphere before the Colima, Mexico, earthquake of 21 January 2003. *Geofísica internacional* **2005**, *44(4)*, 369-377.
31. Shi, K.; Guo, J.; Liu, X.; Liu, L.; You, X.; Wang, F. Seismo-ionospheric anomalies associated with Mw 7.8 Nepal earthquake on 2015 April 25 from CMONOC GPS data. *Geosciences Journal*, **2020**, 1-16.
32. Pulnits, S.; Tsidilina, M.; Ouzounov, D.; Davidenko, D. From Hector Mine M7. 1 to Ridgecrest M7. 1 Earthquake, A Look from a 20-Year Perspective. *Atmosphere* **2021**, *12(2)*, 262.
33. Pulnits, S.; Boyarchuk, K. Ionospheric precursors of earthquakes. *Springer Science & Business Media* **2004**, 31 - 315.
34. Hegai, V. V.; Kim, V. P.; & Liu, J. Y. The ionospheric effect of atmospheric gravity waves excited prior to strong earthquake. *Advances in Space Research* **2006**, *37(4)*, 653-659.
35. Shalimov, S.L. Lithosphere–ionosphere relationship: a new way to predict earthquakes? *Episodes, Intern. Geophys. Newsmag.* **1992**, *15*, 252–254.
36. Liperovsky, V.V.; Pokhotelov, O.A.; Shalimov, S.L. *Ionospheric precursors to earthquake*. Nauka Publ., Moscow, 304 pp. in Russian, 1992.
37. Blanc, E. Observations in the upper atmosphere of infrasonic waves from natural or artificial sources: a summary. *Ann. Geophys.* **1985**, *3*, 673–688.
38. Gokhberg, M.B.; Adushkin, V.V.; Voitov, G.I.; Pushkin, M.G.; Krivomazova, N.G.; Zeldina, B.B. Response of natural gases in Chibine on power industrial explosion. *Doklady Akad. Nauk.* **1998**, *308*, 1082–1086.
39. Gossard, E.E.; Hooke, W.H. *Waves in the Atmosphere*. Elsevier, Amsterdam, 632 pp., 1975.
40. Shalimov, S.L.; Gokhberg, M.B. Lithosphere–ionosphere coupling mechanism and its application for earthquake in Iran on June 20, 1990: 2, Interpretation of the ionospheric effects, in press, 1997.
41. Kamogawa, M. Preseismic lithosphere-atmosphere-ionosphere coupling. *Eos, Transactions American Geophysical Union*, *87(40)*, 417-424.
42. Voitov, G.I.; Dobrovolsky, I.P. Chemical and isotopic carbon instabilities of the native gas flows in seismically active regions. *Physics of the Earth* **1994**, *3*, 20–31.
43. Pulnits, S. A.; Ouzounov, D. P.; Karelin, A. V.; Davidenko, D. V. Physical bases of the generation of short-term earthquake precursors: A complex model of ionization-induced geophysical processes in the lithosphere-atmosphere-ionosphere-magnetosphere system. *Geomagnetism and Aeronomy* **2015**, *55(4)*, 521-538.
44. Pulnits, S. A.; Khagai, V. V.; Boyarchuk, K. A.; Lomonosov, A. M. The atmospheric electric field as a source of variability in the ionosphere. *Uspekhi Fizicheskikh Nauk* **1998**, *168(5)*, 582-589.
45. Mendes, O.J., Domingues, M. O., Costa, A.M.Da., Gonzalez, A.L.C.De. Wavelet analysis applied to magnetograms: Singularity detections related to geomagnetic storms. *J. Atmos. Sol. Terr. Phys.* **2005**, *67*, 17.
46. Adhikari, B.; Dahal, S.; Sapkota, N.; Baruwat, P.; Bhattarai, B.; Khanal, K.; Chapagain, N. P. Field-aligned current and polar cap potential and geomagnetic disturbances: A review of cross-correlation analysis. *Earth and Space Science* **2018**, *5*, 440-455, doi: 10.1029/2018EA000392
47. Poudel, P.; Simkhada, S.; Adhikari, B.; Sharma, D.; Nakarmi, J. J. Variation of solar wind parameters along with the understanding of energy dynamics within the magnetospheric system during geomagnetic disturbances. *Earth and Space Science* **2019**, *6(2)*, 276-293.
48. Silwal, A.; Gautam, S. P.; Poudel, P.; Karki, M.; Adhikari, B. et al.. GPS Observations of Ionospheric TEC Variations during the 15th Jan 2010 and 21st June 2020 Solar Eclipse. *Radio Science*, e2020RS007215.
49. Gonzalez, W.D.; Joselyn, J.A.; Kamide, Y.; Kroehl, H.W.; Rostoker, G. et al. What is a geomagnetic storm?. *Journal of Geophysical Research: Space Physics* **1994**, *99(A4)*, 5771-5792.

50. de Gonzalez, A. L. C.; da Costa, A. M.; Gonzalez, W. D. Ring current space-time inhomogeneities in intense geomagnetic storms. *Geofísica Internacional* **2004**, *43*(2), 205-215.
51. Jankovicová, D.; Dolinský, P.; Valach, F.; & Vörös, Z. Neural network-based nonlinear prediction of magnetic storms. *Journal of Atmospheric and Solar-Terrestrial Physics* **2002**, *64*(5-6), 651-656.
52. Kamide, Y.; Baumjohann, W.; Daglis, I. A.; Gonzalez, W. D.; Grande, M.; Joselyn, J. A. et al. Current understanding of magnetic storms: Storm-substorm relationships. *Journal of Geophysical Research: Space Physics* **1998**, *103*(A8), 17705-17728.
53. Adhikari, B.; Sapkota, N.; Dahal, S.; Bhattarai, B.; Khanal, K.; Chapagain, N.P. Spectral characteristic of geomagnetically induced current during geomagnetic storms by wavelet techniques. *Journal of Atmospheric and Solar-Terrestrial Physics* **2019**, *192*, 104777, doi: 10.1016/j.jastp.2018.01.020.
54. Tsunomura, S. Characteristics of geomagnetic sudden commencement observed in middle and low latitudes. *Earth, planets and space* **1998**, *50*(9), 755-772.
55. Sugiura, M. Equatorial Dst index 1957-1986. *AGA bulletin* **1991**, *40*, 17-38.
56. Kane, R. P. Evolution of Dst and auroral indices during some severe geomagnetic storms. *Revista Brasileira de Geofísica* **2009**, *27*(2), 151-163.
57. Mayaud, P. N. Derivation, meaning, and use of geomagnetic indices. *Washington DC American Geophysical Union Geophysical Monograph Series* **1980**, *22*, 607.
58. Srebrov, B.; Kounchev, O.; Simeonov, G. Wavelet Analysis of Big Data in the Global Investigation of Magnetic Field Variations, in *Solar-Terrestrial Physics*, 2019, arXiv preprint arXiv:1905.12923.
59. Bayer M.; Freeden W.; Maier T. A vector wavelet approach to iono-and magnetospheric geomagnetic satellite data. *Journal of Atmospheric and Solar-Terrestrial Physics* **2001**, *63*(6), 581-97.
60. Khanal, K.; Adhikari, B.; Chapagain, N. P.; Bhattarai, B. HILDCAA-related GIC and possible corrosion Hazard in underground pipelines: A comparison based on wavelet transform. *Space Weather* **2019**, *17*, 238-251, doi: <https://doi.org/10.1029/2018SW001879>
61. Torrence, C.; Compo, G. P. A practical guide to wavelet analysis. *Bulletin of the American Meteorological Society*, **1998**, *79*(1), 61-78, doi: [https://doi.org/10.1175/15200477\(1998\)079<0061:APGTWA>2](https://doi.org/10.1175/15200477(1998)079<0061:APGTWA>2).
62. Mendes da Costa, A.; Domingues, M. O.; Mendes, O.; Brum, C. G.M. Interplanetary medium condition effects in the south Atlantic magnetic anomaly: A case study. *J. Atmos. Sol.Terr. Phy.* **2011**, *73*, 1478-1491.
63. Hafez, A. G.; Ghamrya, E.; Yayamab, H.; and Yumotoe, K. Undecimated discrete wavelet transform based algorithm for extraction of geomagnetic storm sudden commencement onset of high-resolution records. *Comput. Geosci.* **2013**, *51*, 143-152.
64. Klausner, V.; Mendes, O.; Domingues, M. O.; Papa, A. R. R.; Tyler, R. H.; Frick, P.; and Kherani, E. A. Advantage of wavelet technique to highlight the observed geomagnetic perturbations linked to the Chilean tsunami (2010). *J. Geophys. Res.-Space* **2014b**, *119*, 3077-3093.
65. Klausner, V.; Ojeda González, A.; Domingues, M. O.; Mendes, O.; Papa, A. R. R. Study of local regularities in solar wind data and ground magnetograms. *J. Atmos. Sol.-Terr. Phy.* **2014a**, *112*, 10-19.
66. Klausner, V.; Domingues, M.; Mendes, Odim & Papa, Andres. Discrete wavelet analysis of L aquila earthquake 2009 effects on the geomagnetic field. In *Conferência Brasileira de Dinâmica, Controle e Aplicações*, vol. 1, no. único, pp. 719-722. SBMAC, 2011.
67. Ojeda, G.A.; Mendes, O.J.; Domingues, M.O.; Menconi, V.E. Wavelet coefficients: A tool to study interplanetary magnetic fluctuations. *Geofísica int.* **2014**, *53*.
68. Adhikari, B.; Chapagain, N.P. Polar cap potential and merging electric field during high intensity long duration continuous auroral activity. *J. Nepal Phys. Soc.* **2015**, *3*(1), 6, doi: <https://doi.org/10.3126/jnphysoc.v3i1.14437>.
69. Chui, C. *Wavelets: A tutorial in theory and applications*, Academic Press, San Diego, CA 2, 1992.
70. Meyer, Y. *Ondelettes et Operateurs*. Hermann, Paris, 1990.
71. Klausner, V.; Kherani, E. A.; & Muella, M. T. Near-and far-field tsunamigenic effects on the Z component of the geomagnetic field during the Japanese event, 2011. *Journal of Geophysical Research: Space Physics* **2016c**, *121*(2), 1772-1779.
72. Klausner, V.; Papa, A. R. R.; Cândido, C. M. N.; Domingues, M. O.; Mendes, O. An alternative way to identify local geomagnetically quiet days: a case study using wavelet analysis. In *Annales Geophysicae* **2016d**, *34*(4), 451-462, Copernicus GmbH.

73. Schubert, G.; Walterscheid, R.L.; Hickey, M.P.; Tepley, C.A. Observations and interpretation of gravity wave induced fluctuations in the OI (557.7 nm) airglow. *Journal of Geophysical Research: Space Physics* **1999**, *104*(A7), 14915-14924.
74. Medeiros, A.F.; Taylor, M.J.; Takahashi, H.; Batista, P.P.; Gobbi, An investigation of gravity wave activity in the low-latitude upper mesosphere: Propagation direction and wind filtering. *Journal of Geophysical Research: Atmospheres* **2003**, *108*(D14).
75. Wrasse, C.M.; Nakamura, T.; Takahashi, H.; Medeiros, A.F.; Taylor, M.J. et al. Mesospheric gravity waves observed near equatorial and low-middle latitude stations: wave characteristics and reverse ray tracing results. In *Annales Geophysicae* **2006** *24*(12), 3229-3240. Copernicus GmbH.
76. Candido, C.M.N.; Pimenta, A.A.; Bittencourt, J.A.; Becker-Guedes, F. Statistical analysis of the occurrence of medium-scale traveling ionospheric disturbances over Brazilian low latitudes using OI 630.0 nm emission all-sky images. *Geophysical research letters* **2008**, *35*(17).
77. Pimenta, A.A.; Amorim, D.C.M.; Candido, C.M.N. Thermospheric dark band structures at low latitudes in the Southern Hemisphere under different solar activity conditions: A study using OI 630 nm emission all-sky images. *Geophysical research letters* **2008**, *35*(16).
78. Occhipinti, G.; Rolland, L.; Lognonné, P.; Watada, S. From Sumatra 2004 to Tohoku-Oki 2011: The systematic GPS detection of the ionospheric signature induced by tsunamigenic earthquakes. *Journal of Geophysical Research: Space Physics* **2013**, *118*(6), 3626-3636.
79. Tsugawa, T.; Saito, A.; Otsuka, Y.; Nishioka, M.; Maruyama, T. et al. Ionospheric disturbances detected by GPS total electron content observation after the 2011 off the Pacific coast of Tohoku Earthquake. *Earth, planets and space* **2011**, *63*(7), 875-879.
80. Galvan, D.A.; Komjathy, A.; Hickey, M.P.; Stephens, P.; Snively, J.; Song, Y.T.; Butala, M.D.; Mannucci, A.J. Ionospheric signatures of Tohoku-Oki tsunami of March 11, 2011: Model comparisons near the epicenter. *Radio Science* **2012**, *47*(4).
81. Kherani, E.A.; Rolland, L.; Lognonne, P.; Sladen, A.; et al. Traveling ionospheric disturbances propagating ahead of the Tohoku-Oki tsunami: a case study. *Geophysical Journal International* **2015**, *204*(2), 1148-1158.
82. Kherani, E.A.; Lognonne, P.; Hébert, H.; Rolland, L.; Astafyeva, E. Modelling of the total electronic content and magnetic field anomalies generated by the 2011 Tohoku-Oki tsunami and associated acoustic-gravity waves. *Geophysical Journal International* **2012**, *191*(3), 1049-1066.
83. McPherron, R.L. Physical processes producing magnetospheric substorms and magnetic storms. *Geomagnetism* **1991**, *4*, 593-739.
84. Grossmann, A.; Morlet, J. Decomposition of Hardy Functions into Square Integrable Wavelets of Constant Shape. *SIAM Journal on Mathematical Analysis* **1984**, *15*(4), 723-736.
85. Tsurutani, B. T.; Gonzalez, W. D.; Guarnieri, F.; Kamide, Y.; Zhou, X.; Arballo, J. K. Are high-intensity long-duration continuous AE activity (HILDCAA) events substorm expansion events?. *Journal of atmospheric and solar-terrestrial physics* **2004**, *66*(2), 167-176.
86. Lakhina, G. S.; Alex, S.; Tsurutani, B. T.; Gonzalez, W. D. Research on historical records of geomagnetic storms. Proceedings of the International Astronomical Union, 2004(IAUS226), 3-15.
87. Lemaire, J. F. The effect of a southward interplanetary magnetic field on Störmer's allowed regions. *Advances in Space Research* **2003**, *31*(5), 1131-1153.
88. Kumar, P.; Foufoula-Georgiou, E. Wavelet analysis for geophysical applications. *Reviews of Geophysics* **1997**, *35*(4), 385-412, doi: <https://doi.org/10.1029/97RG00427>.